DOI: 10.1002/((please add manuscript number))
Article type: Communication

Stable, High-Sensitivity and Fast-Response Photodetectors Based on Lead-free $Cs_2AgBiBr_6$ Double Perovskite Films

Jie Yang, Chunxiong Bao, Weihua Ning, Bo Wu, Fuxiang Ji, Zhibo Yan, Youtian Tao, Jun-Ming Liu, Tze Chien Sum, Sai Bai, Jianpu Wang, Wei Huang, Wenjing Zhang,* Feng Gao**

Dr. J. Yang, Dr. C. Bao, Prof. W. Zhang
International Collaborative Laboratory of 2D Materials for Optoelectronics Science and Technology, Shenzhen University, Shenzhen 518060, China
E-mail: wjzhang@szu.edu.cn

Dr. J. Yang, Dr. C. Bao, Dr. W. Ning, F. Ji, Dr. Z. Yan, Dr. S. Bai, Prof. F. Gao
Department of Physics, Chemistry, and Biology (IFM) Linköping University, Linköping SE-58183, Sweden
E-mail: sai.bai@liu.se, feng.gao@liu.se

Dr. W. Ning, Prof. Y. Tao, Prof. J. Wang, Prof. W. Huang
Key Lab for Flexible Electronics & Institute of Advanced Materials, Jiangsu National Synergistic Innovation Center for Advanced Materials (SICAM), Nanjing Tech University, 30 South Puzhu Road, Nanjing 211816, P. R. China

Dr. B. Wu, Prof. T. C. Sum
Division of Physics and Applied Physics School of Physical and Mathematical Sciences Nanyang Technological University (NTU)21 Nanyang Link, Singapore 637371, Singapore

Dr. Z. Yan, Prof. J.-M. Liu
Laboratory of Solid State Microstructures and Innovation Center of Advanced Microstructures, Nanjing University, Nanjing 210093, P. R. China

Dr. J. Yang, Dr. C. Bao, Dr. W. Ning
These authors contribute equally to this work

Keywords: lead-free perovskite, $Cs_2AgBiBr_6$, photodetector, fast response, stability

Abstract: Solution-processed metal halide perovskites (MHPs) have demonstrated great advances on achieving highly-sensitive and fast-response photodetectors. However, the intrinsic material instability and the toxicity of the lead still hinder the practical applications of the MHPs-based photodetectors. In this work, we demonstrate the first highly-sensitive and fast-response lead-free perovskite photodetectors based on $Cs_2AgBiBr_6$ double perovskite films. We develop a convenient solution method to deposit high-quality $Cs_2AgBiBr_6$ film with large grain sizes, low trap densities and long charge carrier lifetimes. Incorporated within a photodiode device architecture comprised of optimized hole and electron blocking layers, we achieve lead-free perovskite photodetectors exhibiting a high detectivity of 3.29×10^{12} Jones, a large linear dynamic range of 193 dB and a fast response time of ~17 ns. All the key figures of merits of the devices are comparable with the reported best-performing photodetectors based on lead halide perovskites. In addition, the resulting devices exhibit excellent thermal and environmental stability. The non-encapsulated devices show negligible degradation after thermal stressing under 150 °C and less than 5% degradation in the photoresponsivity after storage in ambient air for ~2300 h. Our results demonstrate the great potential of the lead-free $Cs_2AgBiBr_6$ double perovskite on the applications of environmentally friendly and high-performance photodetectors.

High-performance photodetectors are key components in many important optoelectronic applications, such as optical communications, imaging and photon detection.[1-3] Solution-processed metal halide perovskites (MHPs) have demonstrated large light absorption coefficients, long carrier diffusion lengths, and high carrier mobility, which make them promising semiconductors for the fabrication of photodetectors with high sensitivity and fast response speed. [4-13] Despite the great advances, the intrinsic material instability and the toxicity issue of the commonly used lead halide perovskites hinder their practical applications.[14-16]

Recently, alternative bismuth (Bi) or tin (Sn) based lead-free halide perovskites have been explored for the photodetector applications. [17-19] However, all the reported lead-free perovskite photodetectors show slow response time of milliseconds and poor detectable light intensity of ~μW/cm^2, which still fall behind those based on the well-investigated lead-based perovskites. [6,10,11] In addition, most of the reported lead-free perovskites exhibit poor material stability and/or low charge transport properties, which further hinder their applications in efficient and stable photodetectors.

As a new generation of semiconductors, lead-free double halide perovskites, which exhibit superior material stability and photoelectric properties are ideal for efficient and environmental-friendly optoelectronic applications. [20-27] For example, Tang and co-workers have demonstrated high-performance X-ray detectors with low detection limit based on $Cs_2AgBiBr_6$ double perovskite single crystals.[25] Sensitive and fast UV photodetectors based on $Cs_2AgInCl_6$ single crystals with low trap density have also been reported.[20] However, due to the different solubility of the raw materials in the common organic solvents, cost-effective solution-processing for the fabrication of high-quality double perovskite thin films has been limited and the related optoelectronic devices are rarely reported. [28-31]

Recently, through carefully chosen organic solvent or well-controlled vacuum-assisted processing, uniform $Cs_2AgBiBr_6$ double perovskite thin films have been fabricated and integrated into photodetectors.[21,22] However, the resulting devices with metal-semiconductor-metal (MSM) or heterojunction device structure exhibit low sensitivity and slow response speed, which are mainly due to the large trap density in the perovskite active layer and the non-optimized device structures. In our previous report, we have developed a novel solution-processing method for the deposition of high-quality double perovskite thin films from $Cs_2AgBiBr_6$ single crystal-based precursor solution. The resulting thin films exhibit long and balanced charge carrier diffusion lengths, leading to efficient solar cells with superior stability. [24] However, the films still consist of abundant grain boundaries due to relatively small crystal grain sizes, which induce nonnegligible defects and limit their applications in high-sensitivity and fast-response photodetectors.

In this work, we successfully demonstrate high-crystallinity $Cs_2AgBiBr_6$ films with enlarged grain sizes and reduced trap densities. We further optimize the electron and hole transport interlayers and achieve the first high-sensitivity and fast-response lead-free perovskite photodetector. The resulting devices exhibit a lowest detectable limit of tens of pW/cm^2, and an ultrafast response time of ~17 ns, both of which are comparable to the best-performing photodetectors based on lead halide perovskites. More importantly, the $Cs_2AgBiBr_6$ double perovskite-based photodetectors exhibit superior environmental and device operational stability. For the non-encapsulated devices, we observe negligible degradation in the device performance under thermal stressing at a high temperature of 150 °C and ~94% of the initial photoresponsivity can be retained after storage in ambient air for ~ 2300 h.

We synthesize the $Cs_2AgBiBr_6$ double perovskite single crystals following the developed method in our previous report. [24] We prepare and optimize the precursor solution using a mixture of N,N-Dimethylformamide (DMF) and Methyl sulfoxide (DMSO) as the solvent for the single crystals. We find that the incorporation of a small amount of DMF is helpful to enlarge

the grain size of the obtained $Cs_2AgBiBr_6$ films. **Figure 1a-d** show the top-view scanning electron microscope (SEM) images of the $Cs_2AgBiBr_6$ double perovskite films processed from DMSO-based precursors containing 0%, 5%, 10% and 20% of DMF (v/v) (marked as 0% DP, 5% DP, 10% DP, 20% DP). The $Cs_2AgBiBr_6$ film fabricated from pure DMSO solution exhibits small crystals with an average size of ~250 nm. As the DMF ratio increases to 10%, larger grains with the size over 1 μm appear in the obtained films (**Figure 1b, c**). The results are in good agreement with the obviously increased intensity of the main diffraction peaks of (200) and (400) at 15.71° and 31.76° from the XRD patterns (**Figure 1e**), suggesting the improved crystallinity or orientation of the obtained double perovskite films. As we observe much worse solubility of the double perovskite single crystals in DMF (**Figure S1**), we anticipate that the introduced DMF reduces the nucleation sites and promote the Ostwald ripening of the crystals during the film formation, which is also consistent with previous reported crystal growth of lead halide perovskites.[32] We observe the appearance of some bright area from the SEM images when we further increase the DMF ratio to 20% (**Figure 1d**). According to the XRD characterization results, it can be found that a new diffraction peak locates at 12.7°, which can be attributed to an impurity phase of $Cs_3Bi_2Br_9$.[29,33] **Figure S1** shows that the solubility of AgBr in the DMF/DMSO (20%) solvent is much lower compared with that of CsBr and $BiBr_3$. As a result, the introduced excess DMF may change the stoichiometric molar ratio of CsBr:AgBr:$BiBr_3$ in the precursor solution, inhibiting the AgBr to fit within the crystal lattice and resulting in the formation of $Cs_3Bi_2Br_9$ impurity. We find no obvious changes to the absorption spectra of the resulting films (**Figure S2**). However, we do observe significantly increased photoluminescence (PL) lifetime for the 10% DP film (**Figure 1f**), suggesting the reduced trap densities in the resulting double perovskite films, consistent with the enlarged grain size and improved film crystallinity from the SEM and XRD results.

We investigate the effect of charge transport interlayers on the device performance of the photodetectors. We choose a photodiode device with both electron- and hole-transporting layers

(**Figure 2a**), which has demonstrated great advances in reducing the dark current and improving the response speed of the photodetectors. [6,11] The commonly used n-type metal oxides (TiO_2 and SnO_2) and p-type organic materials of 2,2′,7,7′-tetrakis-(N,N-di-4-methoxyphenylamino)-9,9′-spirobifluorene (Spiro-OMeTAD) and poly [(9,9-dioctylfl uorenyl-2,7-diyl)-co-(4,4′-(N-(4-sec-butylphenyl)diphenylamine)) (TFB) are studied. When the Spiro-OMeTAD is used as the hole-transporting layer (HTL), we measure obviously high dark currents for devices on both TiO_2 and SnO_2 electron-transporting layer (ETL) (**Figure 2b**). In contrast, the devices with TFB as the HTL exhibit significantly lower dark current under the same bias condition. We measure a dark current of 1.0×10^{-4} mA cm^{-2} at -0.2 V for devices processed on the SnO_2 substrate with TFB as the HTL, which is much lower than previous reported MSM devices and is comparable with the well-investigated lead-based perovskite photodetectors.[9,10] Considering the same active layer thickness and absorption (**Figure S2**) and the similar energy level structures (**Figure S3**) of the charge transport interlayers in the device structures, we anticipate that the observed difference in the dark current may origin from the different trap densities in the devices. The reason for Vo not centered at O V is probably the voltage induced ions drift in $Cs_2AgBiBr_6$.

In order to obtain further information on the trap densities, we perform capacitance spectra measurement of the devices with different charge transport interlayers. The difference of the capacitance at different frequencies reflects the electrical active defect state properties of the $Cs_2AgBiBr_6$ films.[34] **Figure 2(c)** shows the measured capacitance results of the three devices at 300 K. The measured capacitance at low and high frequency of devices with Spiro-OMeTAD as HTL are much larger than those of devices with TFB as the HTL, indicating more serious trap states with Spiro-OMeTAD HTL. We further conduct the capacitance measurements at different temperatures to reveal the trap density distribution in the devices (**Figure S6**). Based on the characterization results, trap density of state (tDOS) of the devices with different structures can be calculated as shown in **Figure 2(d)**.[34,35] The tDOS of the devices with Spiro-

OMeTAD as the HTL are ~10^{22} $m^{-3}eV^{-1}$ and ~10^{23} $m^{-3}eV^{-1}$ based on SnO_2 and TiO_2, respectively, which suggests that there may exist more defects at the interfaces of double perovskite/TiO_2. Further replacing the Spiro-OMeTAD with TFB, the tDOS decreases by nearly two orders of magnitude. This is a surprising result, which indicates that the TFB is likely to introduce a further passivation of the defects at the surface of the obtained double perovskite films, and is consistent with the previous demonstrated passivation effects of TFB for lead-halide perovskites.[36]

Having established the optimized device structure, we now evaluate the key device parameters of the $Cs_2AgBiBr_6$ double perovskite photodetectors with the SnO_2 and TFB as the ETL and HTL, respectively. **Figure 3a** shows the typical photocurrent and dark current density–voltage (J–V) curve of $Cs_2AgBiBr_6$ photodetectors fabricated with 10% DMF. The scan rate is 0.2V/s. Linear I-V curve in **Figure S5** showed the device no obvious hysteresis. The photocurrent and dark J–V curves for $Cs_2AgBiBr_6$ photodetectors fabricated with 0%, 5%, 10% and 20% DMF are shown in **Figure S6(a)**. One can observe that the addition of DMF in precursor solution plays a crucial role in the photocurrent enhancement, with the highest short-circuit current (J_{SC}) of 1.1 mA/cm^2 for photodetector processed from 10% DP. The result is further evidenced with the measured higher external quantum efficiency (EQE) measured under 0 V bias (**Figure 3b and Figure S6(b)**), which we attribute to the better crystallinity and reduced trap density of the double perovskite active layer. For the material $Cs_2AgBiBr_6$ has a absorption peak around 450 nm as seen in Figure S2, and the ITO substrate would absorb partial light under 350 nm, the EQE spectra of the devices exhibit two peaks. The optimized device shows a small dark current noise of ~10 fA $Hz^{-1/2}$ at high frequency at 0V bias (**Figure 3c**), while the instrument noise current is around 2 fA $Hz^{-1/2}$, which demonstrates that the measured noise is mainly from the device. Based on the EQE curves and the device noise current at high

frequency, we calculate the device responsivity (R) and specific detectivity (D*) according to the following calculations:

$$R=\frac{J_{ph}}{L_{light}}=\frac{EQE\cdot\lambda}{1240} \quad (1)$$

$$D^{*}=\frac{J_{ph}/L_{light}}{(2qJ_{d})^{1/2}} \quad (2)$$

where J_{ph} is the photocurrent, L_{light} is the incident light intensity, q is the elementary charge, EQE is the external quantum efficiency of the photodetector, λ (nm) is the wavelength of incident light, J_d is the dark current. The values were calculated to be 0.14 A/W and 3.29×10^{12} Jones at 445 nm, which we plot in **Figure 3d**. The noise current which is used to determine the detectivity is the measured lowest noise current under 655 Hz frequency. We note that the detectivity of our optimized device surpasses all the lead-free perovskite photodetectors. [15,17-20] In addition, it is also comparable to the devices based on lead halide perovskites [6,11] and the commercial Si photodiode at the same wavelength, demonstrating its potential application in the detection of blue light.

We now investigate the linear dynamic range (LDR), which is an important characteristic for the photodetector and can be used to determine the detectable light intensity range. We calculate the LDR of our devices based on the linearly detectable light intensity or linear photocurrent.

$$\mathrm{LDR}=20lg\frac{P_{max}}{P_{min}}=20lg\frac{J_{max}}{J_{min}}$$

where the P_{max} (P_{min}) is the maximum (minimum) light intensity that a photodetector can linearly response to, the J_{max} (J_{min}) is the maximum (minimum) linear response photocurrent of a photodetector. The photocurrent of the device as a function of the light intensity is provided in **Figure 3e**. We observe that our optimized photodetectors based on the $Cs_2AgBiBr_6$ double perovskite show a linear response range from a light intensity of 2×10^{-11} to 0.15 W cm^{-2}, corresponding to a large LDR of 193.4 dB. This value compares favorably with that of the best-

performing lead halide perovskite photodetectors based on $CH_3NH_3PbI_{3-x}Cl_x$ thin film (>100 dB) or $CH_3NH_3PbI_3$ single crystals (222 dB) and even larger than the commercially available Si (120 dB) or InGaAs based (66 dB) photodetectors.

We further study the response speed of the double perovskite photodetectors by measuring the transient photocurrent when applying a 4 ns wide pulse laser (337 nm) to excite the photodetectors. **Figure S7a** shows the transient photocurrent curves of the double perovskite photodetectors fabricated with perovskite precursor with different DMF ratio. By fitting the decay curves with the exponential decay function, the response time of the devices are obtained. A fastest response speed of about 164 ns can be obtained for the optimized device based on 10% DP. The response speed of the double perovskite photodetectors based on different charge blocking layers are also compared, which are given in **Figure S7b**. The $Cs_2AgBiBr_6$ photodetectors with TiO_2/Spiro-OMeTAD and SnO_2/Spiro-OMeTAD as charge blocking layers show large response time over 1 μs, while the devices with TFB HTL show much faster response of ~ 200 ns. It has been demonstrated that the resistance-capacitance (RC) constant, which is related to the defects in the devices, is a crucial factor determining the response speed of a photodetector. [7,11] As a result, the fastest response speed is observed for the optimized devices based on perovskite film fabricated with DMF ratio of 10% and SnO_2/TFB charge transport layers. Meanwhile, a further improved response speed is obtained based on smaller-area devices, which is consistent with the decreased devices capacitance. As shown in **Figure 3f**, an ultrafast response speed of ~17 ns can be obtained for a device with an active area of ~0.2 mm^2, which represents the fastest lead-free perovskite photodetector and is comparable with the best-performing lead-based perovskite photodetectors reported so far (as shown in **Table 1**). [11,20-22]

Finally, we proceed to investigate the device operational stability, which is critically important for practical applications of the photodetectors. We first study the device operational stability of the $Cs_2AgBiBr_6$ photodetectors by monitoring the change of the photocurrent under

different temperature with a blue LED light illumination. The devices are placed on a hot plate in ambient air condition (T: 20 °C, RH: ~40%) without encapsulation. A $CH_3NH_3PbI_3$ ($MAPbI_3$) photodetector with the same device structure is investigated simultaneously as a control for the stability comparison.

As we show in **Figure 4a** of the device stability performance, the photocurrent of the $Cs_2AgBiBr_6$ photodetector keeps constant in the initial 1 h operational test under room temperature, while the $MAPbI_3$ photodetector experiences slow degradation, indicating a better stability of $Cs_2AgBiBr_6$ device under 450 nm illumination in ambient with light intensity of 10 μ W/cm^2. We then increase the temperature of the hot plate to 150 °C and keep measuring the devices for another 1 hour. We discover that the photocurrents of both photodetectors quickly decrease to about half of the initial values (**Figure 4a**), which is properly due to the increase of non-radiative recombination in the semiconductors under a high temperature.[37] The photocurrent of $Cs_2AgBiBr_6$ photodetectors becomes steady in about 20 min after the temperature increase to 150 °C, while a continuous decay is observed for $MAPbI_3$ photodetectors. After we cool the hot plate to room temperature, the photocurrent of $Cs_2AgBiBr_6$ photodetectors go back to its original value. However, the $MAPbI_3$ photodetectors shows nonreversible degradation in the device performance, which is due to the well-known decomposition of the $MAPbI_3$ active layer under elevated temperature.[38,39] The results suggest superior thermal stability of the $Cs_2AgBiBr_6$ double perovskite active layer and the resulting photodetectors. The current is normalized to help see the stability trend of different devices easily. The real current has been given in Figure S8. We also investigate the long-term device operational stability in ambient air under light illumination for 10 h and show the results in **Figure 4b**. We observe that the $Cs_2AgBiBr_6$ double perovskite photodetectors shows almost constant device performance during the whole test. We further demonstrate the great environmental stability of

the obtained double perovskite devices (18 devices), with 94% of its initial photoresponsivity retained after storing under ambient condition (RH: ~40%) for 2300 hours (**Figure 4c**).

In summary, we have demonstrated the first high-sensitivity and fast-response lead-free perovskite photodetectors based on high-crystallinity $Cs_2AgBiBr_6$ double perovskite with an optimized photodiode device structure. The resulting devices exhibit a high specific detectivity of 3.29×10^{12} Jones, a high linear dynamic range of 193 dB and a fast response time of ~17 ns, representing the best-performing lead-free perovskite photodetectors so far. Moreover, we demonstrated the superior operational, thermal and environmental stability of the resulting devices, suggesting the great advances of the $Cs_2AgBiBr_6$ double perovskite photodetectors for the applications under harsh conditions.

Experimental Section

Materials: All the materials were used as received without further purification. The materials used in our work are as follows: 15% SnO_2 colloid precursor (Alfa Aesar), 97% titanium isopropoxide (Sigma-Aldrich), CsBr (99.9%, Alfa Aesar), AgBr (99.999%, Sigma-Aldrich), BiBr3 (≥98%, Sigma-Aldrich), 47% HBr aqueous solution, anhydrous DMSO (Sigma-Aldrich), anhydrous DMF (Sigma-Aldrich), TFB (poly(9,9-dioctyl-fluorene-co-N-(4-butylphenyl)diphenylamine), Sigma-Aldrich), spiro-OMeTAD (Sigma-Aldrich), Li-TFSI (Lithium bis(trifluoromethanesulfonyl)imide, Sigma-Aldrich), tert-butylpyridine (96%, Sigma-Aldrich).

$Cs_2AgBiBr_6$ Single Crystals Synthesis: 213 mg CsBr, 225 mg $BiBr_3$, and 94 mg AgBr were added in 8 mL of 47% HBr aqueous solution. The mixture was heated to 120 °C until the materials were totally dissolved. Then the solution was cooled to room temperature slowly (in ~12 hours). Red $Cs_2AgBiBr_6$ octahedral single crystals can be obtained with size up to $4 \times 4 \times 2$ mm^3.

Photodetectors Fabrication: The SnO_2 film precursor solution was prepared by diluting 15% (wt%) SnO_2 nanocrystal colloidal solution (Alfa Aesar) in deionized water to 2.67% (wt%).

SnO_2 precursor solution was spin-coated onto an ITO substrate at 4000 rpm for 30 s, followed by annealing at 150 °C for 0.5 h. 0.5 M $Cs_2AgBiBr_6$ precursor solution were prepared by dissolving the $Cs_2AgBiBr_6$ single crystals in DMSO/DMF mixed solvents at 150 °C with the DMF ratios of 0%, 5%, 10% and 20%, respectively. The time of dissolving depends on the amount of DMF in the solution. For 5%, 10%, 20% DMF, the single crystals dissolving time is about 2 min, 5 min and 8 min, respectively. After the solution was decreased to room temperature, $Cs_2AgBiBr_6$ films were deposited onto the SnO_2/ITO substrates at 4000 rpm for 60 s and annealed at 250 °C for 10 min to obtain better crystallization. The TFB precursor solution was prepared by dissolving 12 mg TFB in 1 mL chlorobenzene. The TFB hole transport layer was spin-coated on the $Cs_2AgBiBr_6$ films at 3000 rpm for 30s. Finally, a 7 nm MoO_3 layer and an 80 nm gold layer were deposited by thermal evaporation at a pressure of 1×10^{-4} mbar. TiO_2 compact layers were fabricated by spin-coating an acid titanium isopropoxide ethanol solution at 5000 rpm for 20s, followed by annealing at 200 °C for 2 h. Spiro-OMeTAD hole transport layer was fabricated by spin-coating a chlorobenzene solution (72.3 mg spiro-MeOTAD, 17.5 μL Li-TFSI in acetonitrile (520 mg/ml), 28.8 mL tert-butylpyridine (TBP) in 1 mL chlorobenzene) at 3000 rpm for 30 s.

Device Characterization: The morphologies of $Cs_2AgBiBr_6$ film were characterized with SEM (LEO 1550). XRD patterns were measured with X-ray diffractometer (X'Pert PRO) with the wavelength of 1.5406 Å. Ultraviolet–visible absorption spectra for different $Cs_2AgBiBr_6$ films were measured with Shimadzu spectrophotometer (UV-2450). The current density–voltage (J–V) curves were measured by recording the photocurrent and dark current with 2400 Series Source Meter (Keithley). The light used for J-V curves measurement was an AM 1.5 Solar Simulator. The effective area for every device cell was defined to be 7.25 mm^2. The external quantum efficiency (EQE) curves were measured by a spectral response measurement system (QE-R3011, Enli Technology Co. Ltd) at zero bias voltage with the incident monochrome light calibrated by a standard Si photovoltaic cell. Time-resolved photoluminescence (TRPL) was

used to characterize the electrodes charge carrier dynamics using 400 nm femtosecond excitation pulses (50 fs). The noise current was recorded by a lock-in amplifier (SR830). Transient photocurrent was recorded by an oscilloscope with input resistances of 50 Ω. The incident pulse laser wavelength was chosen to be 337 nm with the pulse width of 4 ns.

Supporting Information
Supporting Information is available from the Wiley Online Library or from the author.

Acknowledgements

This work is financially supported by the National Natural Science Foundation of China (51472164), the 1000 Talents Program for Young Scientists of China, Shenzhen Peacock Plan (KQTD2016053112042971), the Educational Commission of Guangdong Province (2015KGJHZ006, 2016KCXTD006), the Science and Technology Planning Project of Guangdong Province (2016B050501005), a China Postdoctoral Science Foundation (2017M622744, 2018T110886), the Swedish Research Council FORMAS (942-2015-1253), the European Commission Marie Skłodowska-Curie Actions (691210), and the Swedish Government Strategic Research Area in Materials Science on Functional Materials at Linköping University (Faculty Grant SFO-Mat-LiU no. 2009-00971).

Received: ((will be filled in by the editorial staff))
Revised: ((will be filled in by the editorial staff))
Published online: ((will be filled in by the editorial staff))

References

[1] H. Melchior, M. B. Fisher, F. R. Arams, *Proc. IEEE* **1970**, *58*, 1466.

[2] E. R. Fossum, *IEEE Trans. Electron Devices* **1997**, *44*, 1689.

[3] M. Akiba, K. Tsujino, M. Sasaki, *Opt. Lett.* **2010**, *35*, 2621.

[4] S. D. Stranks, G. E. Eperon, G. Grancini, C. Menelaou, M. J. P. Alcocer, T. Leijtens, L. M. Herz, A. Petrozza, H. J. Snaith, *Science* **2013**, *342*, 341.

[5] D. Shi, V. Adinolfi, R. Comin, M. Yuan, E. Alarousu, A. Buin, Y. Chen, S. Hoogland, A. Rothenberger, K. Katsiev, Y. Losovyj, X. Zhang, P. A. Dowben, O. F. Mohammed, E. H. Sargent, O. M. Bakr, *Science* **2015**, *347*, 519.

[6] L. Dou, Y. (Micheal) Yang, J. You, Z. Hong, W.-H. Chang, G. Li, Y. Yang, *Nat. Commun.* **2014**, *5*, 5404.

[7] Q. Lin, A. Armin, D. M. Lyons, P. L. Burn, P. Meredith, *Adv. Mater.* **2015**, *27*, 2060.

[8] C. Bao, W. Zhu, J. Yang, F. Li, S. Gu, Y. Wang, T. Yu, J. Zhu, Y. Zhou, Z. Zou, *ACS Appl. Mater. Interfaces* **2016**, *8*, 23868.

[9] J. Yang, T. Yu, K. Zhu, Q. Xu, *J. Phys. D. Appl. Phys.* **2017**, *50*, 495102.

[10] C. Bao, Z. Chen, Y. Fang, H. Wei, Y. Deng, X. Xiao, L. Li, J. Huang, *Adv. Mater.* **2017**, *29*, 1703209.

[11] C. Bao, J. Yang, S. Bai, W. Xu, Z. Yan, Q. Xu, J. Liu, W. Zhang, F. Gao, *Adv. Mater.* **2018**, *30*, 1803422.

[12] H. Wang and D. H. Kim, *Chem. Soc. Rev.* **2017**, *46*, 5204—5236.

[13] F. P. G. Arquer, A. Armin, P. Meredith, E. H. Sargent, *Nature Reviews Materials* **2017**, *2*, 16100.

[14] D. Bryant, N. Aristidou, S. Pont, I. Sanchez-Molina, T. Chotchunangatchaval, S. Wheeler, J. R. Durrant, S. A. Haque, *Energy Environ. Sci.* **2016**, *9*, 1655.

[15] M. Lyu, J. H. Yun, P. Chen, M. Hao, L. Wang, *Adv. Energy Mater.* **2017**, *7*, 1602512.

[16] T. Leijtens, G. E. Eperon, N. K. Noel, S. N. Habisreutinger, A. Petrozza, H. J. Snaith, *Adv. Energy Mater.* **2015**, *5*, 1500963.

[17] C. Ji, P. Wang, Z. Wu, Z. Sun, L. Li, J. Zhang, W. Hu, M. Hong, J. Luo, *Adv. Funct. Mater.* **2018**, *28*, 1705467.

[18] X. W. Tong, W. Y. Kong, Y. Y. Wang, J. M. Zhu, L. B. Luo, Z. H. Wang, *ACS Appl. Mater. Interfaces* **2017**, *9*, 18977.

[19] A. Waleed, M. M. Tavakoli, L. Gu, Z. Wang, D. Zhang, A. Manikandan, Q. Zhang, R. Zhang, Y.-L. Chueh, Z. Fan, *Nano Lett.* **2017**, *17*, 523.

[20] J. Luo, S. Li, H. Wu, Y. Zhou, Y. Li, J. Liu, J. Li, K. Li, F. Yi, G. Niu, J. Tang, *ACS Photonics* **2018**, *5*, 398.

[21] L.-Z. Lei, Z.-F. Shi, Y. Li, Z.-Z. Ma, F. Zhang, T.-T. Xu, Y.-T. Tian, D. Wu, X.-J. Li, G.-T. Du, *J. Mater. Chem. C* **2018**, *6*, 7982.

[22] L. X. C. Wu, B. Du, W. Luo, Y. Liu, T. Li, D. Wang, X. Guo, H. Ting, Z. Fang, S. Wang, Z. Chen, Y. Chen, *Adv. Opt. Mater.* **2018**, *6*, 1800811.

[23] G. Volonakis, A. A. Haghighirad, R. L. Milot, W. H. Sio, M. R. Filip, B. Wenger, M. B. Johnston, L. M. Herz, H. J. Snaith, F. Giustino, *J. Phys. Chem. Lett.* **2017**, *8*, 772.

[24] W. Ning, F. Wang, B. Wu, J. Lu, Z. Yan, X. Liu, Y. Tao, J. M. Liu, W. Huang, M. Fahlman, L. Hultman, T. C. Sum, F. Gao, *Adv. Mater.* **2018**, *30*, 1706246.

[25] W. Pan, H. Wu, J. Luo, Z. Deng, C. Ge, C. Chen, X. Jiang, W.-J. Yin, G. Niu, L. Zhu, L. Yin, Y. Zhou, Q. Xie, X. Ke, M. Sui, J. Tang, *Nat. Photonics* **2017**, *11*, 726.

[26] C. Bi, Q. Wang, Y. Shao, Y. Yuan, Z. Xiao, J. Huang, *Nat. Commun.* **2015**, *6*, 7747.

[27] H. Do Kim, H. Ohkita, H. Benten, S. Ito, *Adv. Mater.* **2016**, *28*, 917.

[28] W. Gao, C. Ran, J. Xi, B. Jiao, W. Zhang, M. Wu, X. Hou, Z. Wu, *ChemPhysChem* **2018**, *19*, 1696.

[29] E. Greul, M. L. Petrus, A. Binek, P. Docampo, T. Bein, *J. Mater. Chem. A* **2017**, *5*, 19972.

[30] C. Wu, Q. Zhang, Y. Liu, W. Luo, X. Guo, Z. Huang, H. Ting, W. Sun, X. Zhong, S. Wei, S. Wang, Z. Chen, L. Xiao, *Adv. Sci.* **2017**, *5*, 1700759.

[31] M. L. M. Wang, P. Zeng, S. Bai, J. Gu, F. Li, Z. Yang, *Sol. rrl* **2018**, *2*, 1800217.

[32] H. Ko, D. H. Sin, M. Kim, K. Cho, *Chem. Mater.* **2017**, *29*, 1165.

[33] Y. Lou, M. Fang, J. Chen, Y. Zhao, *Chem. Commun.* **2018**, *54*, 3779.

[34] H. Duan, H. Zhou, Q. Chen, P. Sun, S. Luo, T. Song, B. Bob, Y. Yang, *Phys. Chem. Chem. Phys.* **2014**, *17*, 112.

[35] M. Samiee, S. Konduri, B. Ganapathy, R. Kottokkaran, H. A. Abbas, A. Kitahara, M. Samiee, S. Konduri, B. Ganapathy, R. Kottokkaran, *Appl. Phys. Lett.* **2014**, *105*, 153502.

[36] Z. Zhu, Y. Bai, H. K. H. Lee, C. Mu, T. Zhang, L. Zhang, J. Wang, H. Yan, S. K. So, S. Yang, *Adv. Funct. Mater.* **2014**, *24*, 7357.

[37] G. J. A. H. Wetzelaer, M. Scheepers, A. M. Sempere, C. Momblona, J. Ávila, H. J. Bolink, *Adv. Mater.* **2015**, *27*, 1837.

[38] B. Conings, J. Drijkoningen, N. Gauquelin, A. Babayigit, J. D'Haen, L. D'Olieslaeger, A. Ethirajan, J. Verbeeck, J. Manca, E. Mosconi, F. De Angelis, H. G. Boyen, *Adv. Energy Mater.* **2015**, *5*, 1500477.

[39] S. Bai, Z. Wu, X. Wu, Y. Jin, N. Zhao, Z. Chen, Q. Mei, X. Wang, Z. Ye, T. Song, R. Liu, S. tong Lee, B. Sun, *Nano Res.* **2014**, *7*, 1749.

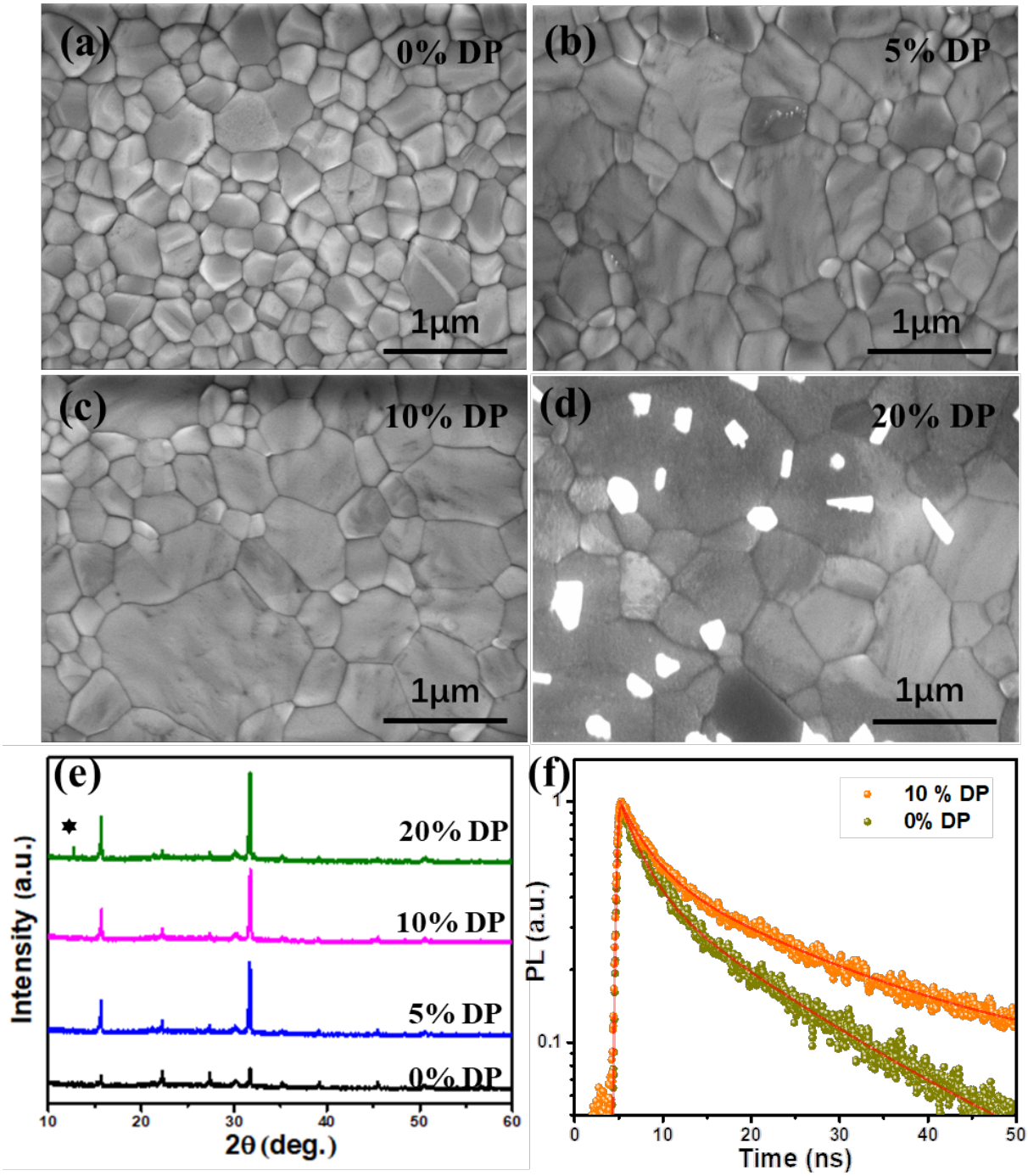

Figure 1 (a-d) Scanning electron microscope (SEM) images of the $Cs_2AgBiBr_6$ films fabricated with solvents containing different DMF ratio of 0%, 5%, 10% and 20%. (e) X-ray diffraction (XRD) patterns of $Cs_2AgBiBr_6$ films fabricated with solvents containing different DMF ratio of 0%, 5%, 10% and 20%. The peak marked with asterisk for the 20% XRD pattern indicates the side phases $Cs_3Bi_2Br_9$ (ICDD no. 01-070-0493). (f) Time-resolved photoluminescence (TRPL) of the $Cs_2AgBiBr_6$ electrodes fabricated with fabricated with 10% DMF ratio and without DMF.

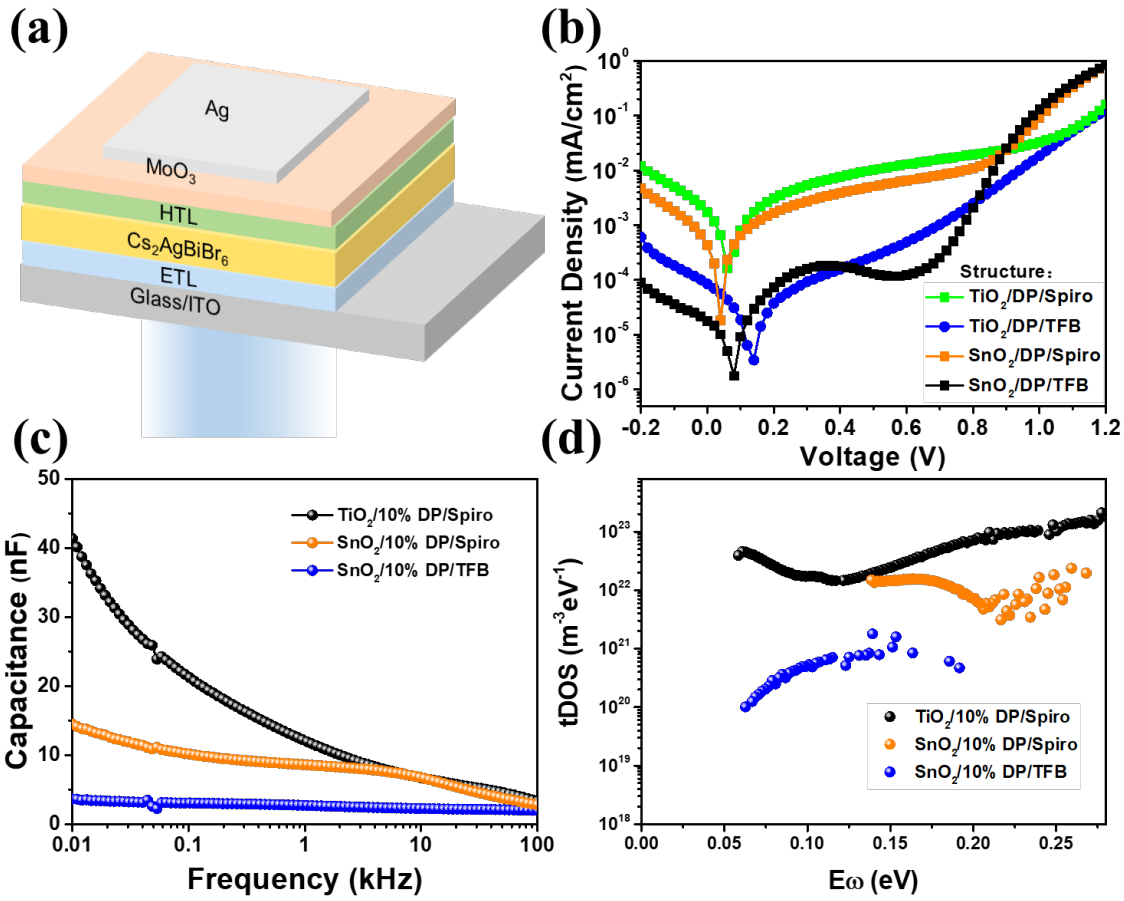

Figure 2 (a) Schematic structure of the photodiode type photodetector with $Cs_2AgBiBr_6$ as light absorber layer. (b) Dark current density-voltage curves of the $Cs_2AgBiBr_6$ photodetectors based on different charge transport layers with $Cs_2AgBiBr_6$ fabricated with 10% DMF. (c) Capacitance spectra of $Cs_2AgBiBr_6$ photodetectors based on different charge transport layers and double perovskite films fabricated with 10% DMF. (d) Trap density of $Cs_2AgBiBr_6$ photodetectors based on different charge transport layers and double perovskite films fabricated with 10% DMF.

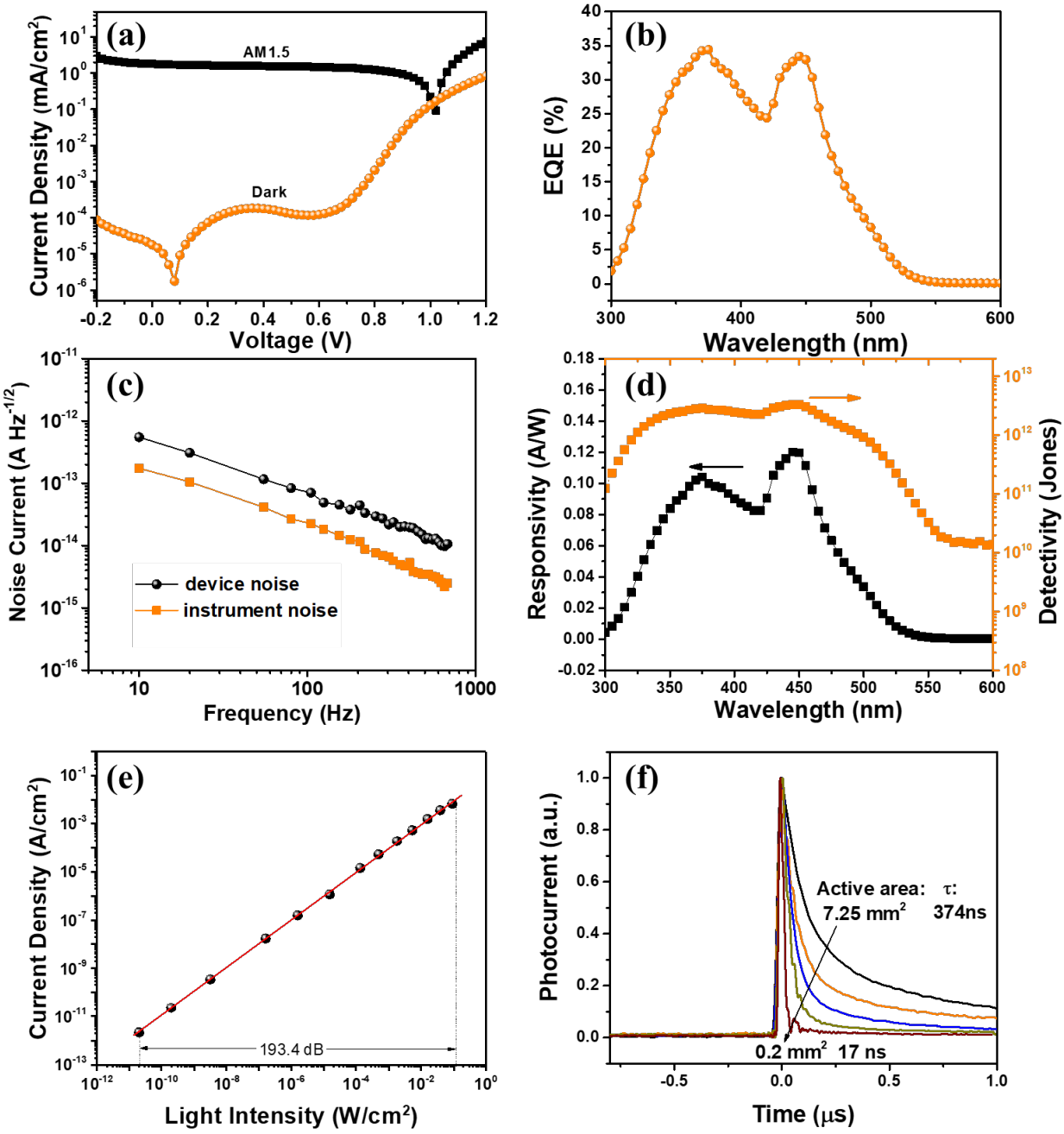

Figure 3 (a) Current density–voltage (J–V) curves of the $Cs_2AgBiBr_6$ photodetectors fabricated with DMF ratio of 10% under dark and AM1.5 illumination. (b) EQE curves under 0 V bias of the $Cs_2AgBiBr_6$ photodetectors fabricated with DMF ratio of 10%. (c) Noise current under 0 V bias of the $Cs_2AgBiBr_6$ photodetectors fabricated with 10% DMF concentration and instrument noise current. (d) Responsivity and detectivity under 0 V bias of the $Cs_2AgBiBr_6$ photodetectors fabricated with 10% DMF concentration. (e) LDR of the $Cs_2AgBiBr_6$ photodetectors fabricated with 10% DMF concentration measured under light wavelength of 450 nm. (f) Transient photocurrent under 0 V bias of the $Cs_2AgBiBr_6$ photodetectors with different active area from 7.25 mm^2 to 0.2 mm^2.

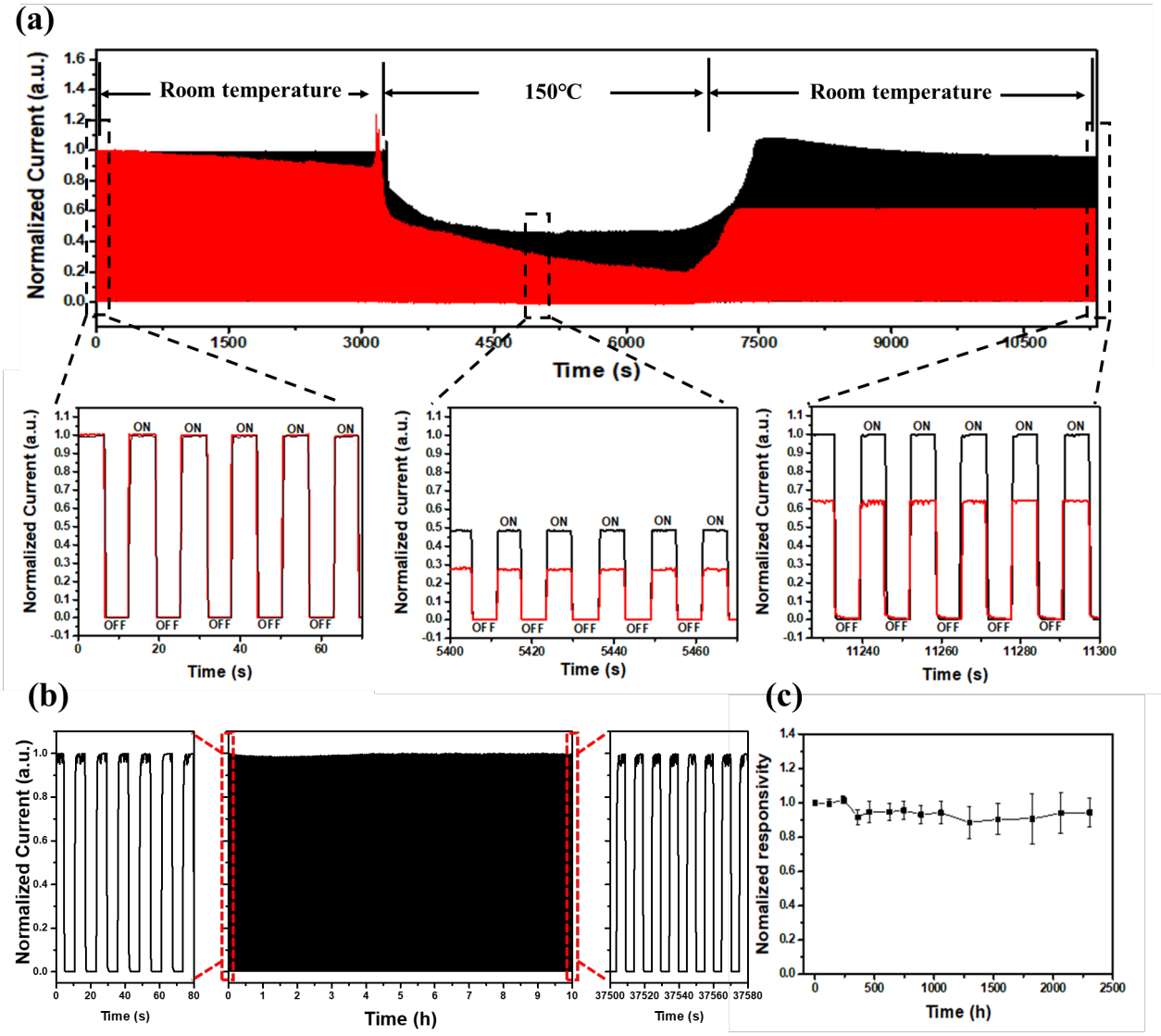

Figure 4 (a) Thermal stability of the $Cs_2AgBiBr_6$ photodetector (black curve) and the $MAPbI_3$ photodetector (red curve) under light wavelength of 450 nm with the intensity of 10 μ W/cm^2. (b)10 h of operation stability and (c) Long-term air stability for 2300 h of the $Cs_2AgBiBr_6$ photodetectors.

Table 1. Summary of the key device parameters of some reported perovskite photodetectors.

	Structure [a]	D* [cm W^{-1} $Hz^{1/2}$]	response time	Stability	Ref
Lead-based	PEDOT:PSS/$MAPbI_{3-x}Cl_x$/PCBM	--	160 ns	--	[6]
	PEDOT:PSS/$MAPbI_3$/PCBM/C_{60}	$>10^{12}$	1 μs	--	[7]
	PTAA/$MAPbBr_3$ SC/C_{60}/BCP	1.5×10^{13}	100 ns	--	[10]
	PTAA/PEIE/$CsPbIBr_2$/PCBM/BCP	9.7×10^{12}	20 ns	>2000 h	[11]
Lead-free	Au/$Cs_2AgInCl_6$ SC/Au	9.6×10^{11}	~1.0 ms	--	[18]
	Au/(TMHD)$BiBr_5$ SC/Au	--	10.3 ms	--	[15]
	Al/$MASnI_3$/Au	8.8×10^{10}	0.4 s	--	[17]
	Au/$Cs_2AgInCl_6$/Au	5.7×10^{11}	1.0 ms	>2 weeks	[19]
	SnO_2/$Cs_2AgBiBr_6$/Au	2.4×10^{10}	~2.0 ms	~180 days	[20]
	SnO_2/$Cs_2AgBiBr_6$/TFB/Au	3.3×10^{12}	17 ns	>2300 h	This work

[a] PCBM: [6,6]-Phenyl C_{61} butyric acid methyl ester, SC: single crystal, BCP: Bathocuproine, TMHD: N,N,N,N-tetramethyl-1,6-hexanediammonium, MA:CH_3NH_3

Supporting Information

Stable, High-Sensitivity and Fast-Response Photodetectors Based on Lead-free $Cs_2AgBiBr_6$ Double Perovskite Films

Jie Yang, Chunxiong Bao, Weihua Ning, Bo Wu, Fuxiang Ji, Zhibo Yan, Youtian Tao, Jun-Ming Liu, Tze Chien Sum, Sai Bai, Jianpu Wang, Wei Huang, Wenjing Zhang,* Feng Gao**

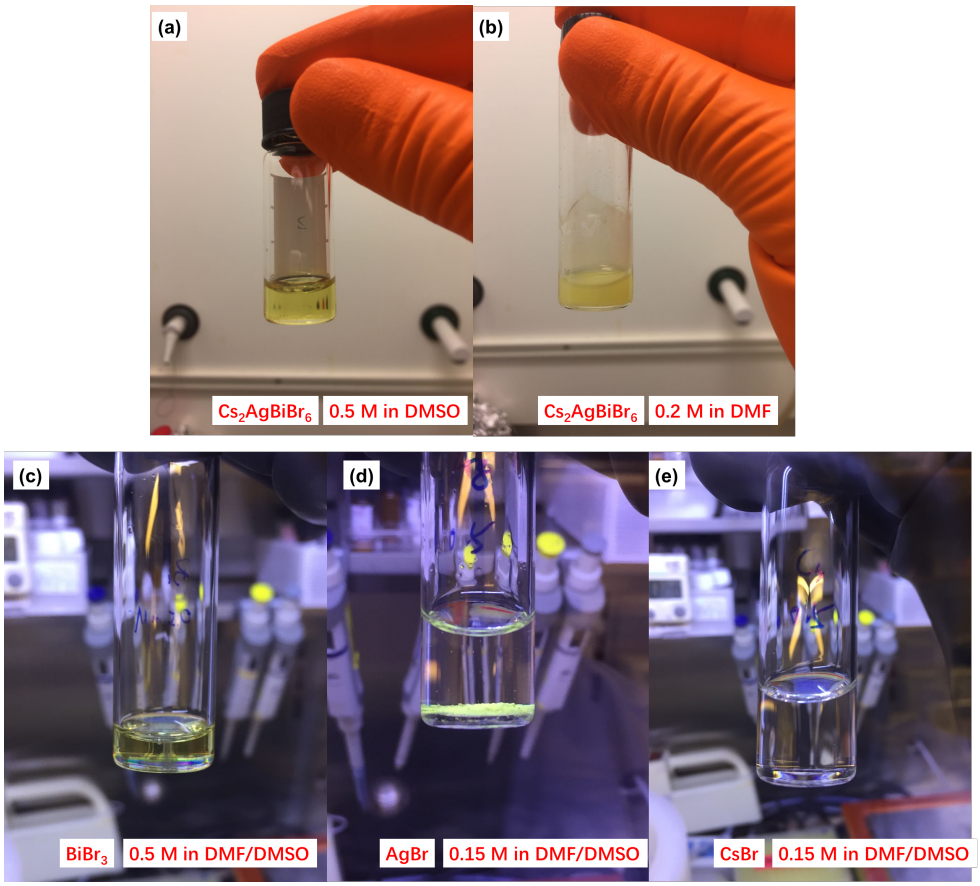

Figure S1 Digital photographs of $Cs_2AgBiBr_6$ and its precursors in DMSO, DMF and their mixture solvent (DMF/DMSO=20 vol%).

.

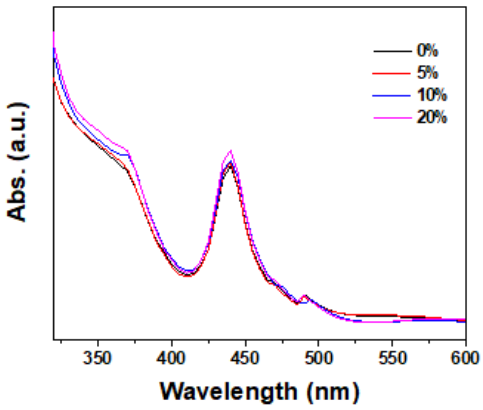

Figure S2 Light absorption spectra of the $Cs_2AgBiBr_6$ films fabricated with solvents containing different DMF ratio of 0%, 5%, 10% and 20%.

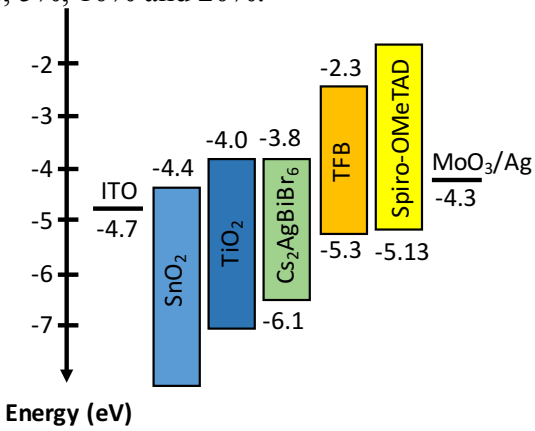

Figure S3 Energy diagram of each layer in $Cs_2AgBiBr_6$ photodetectors.

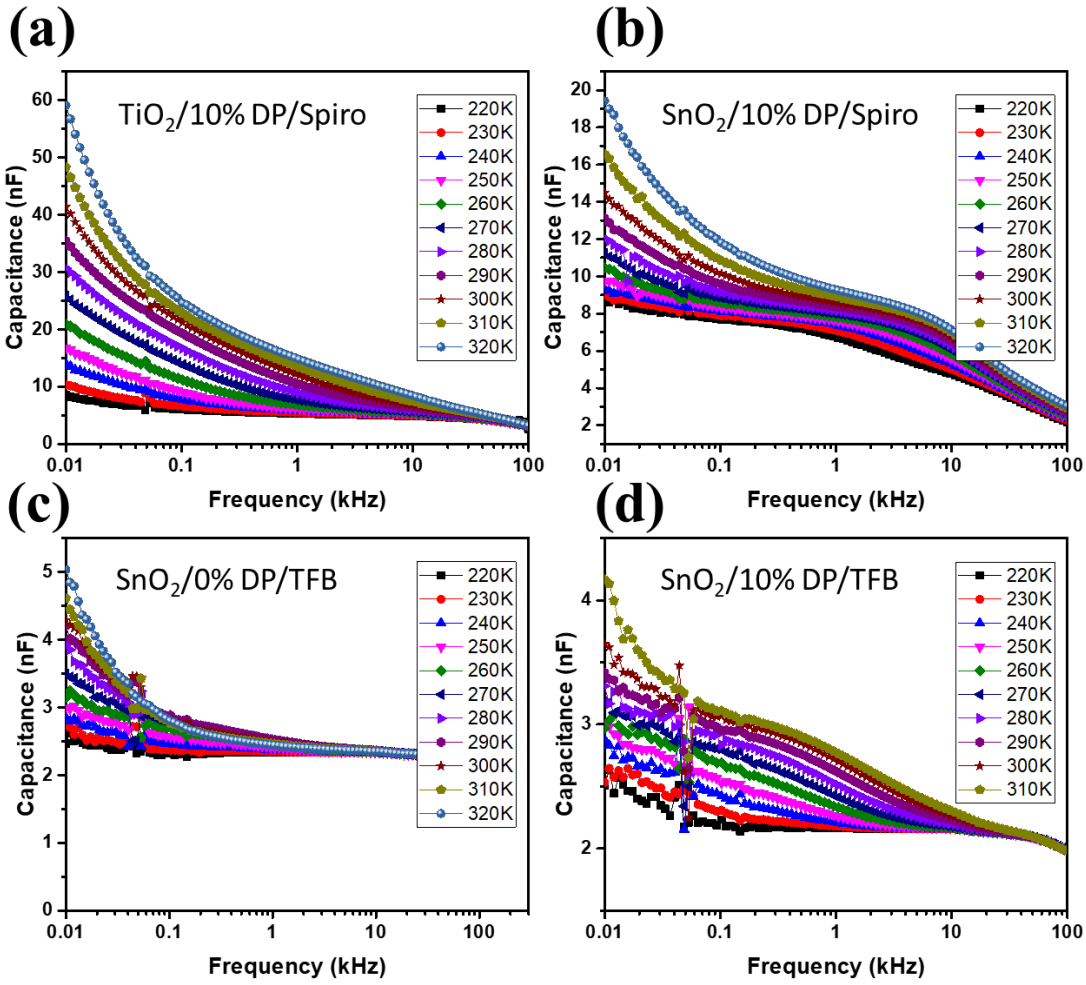

Figure S4 Capacitance spectra at different temperature different devices.

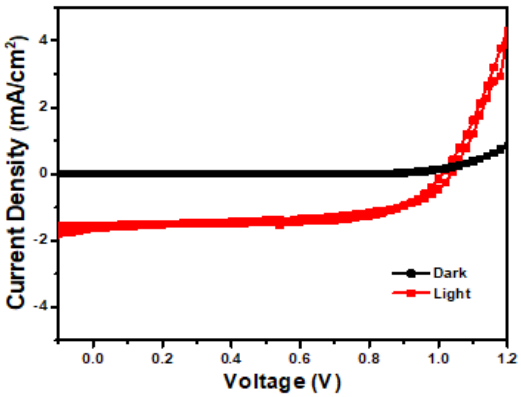

Figure S5 Linear J-V curves of the $Cs_2AgBiBr_6$ photodetector fabricated with 10%DMF.

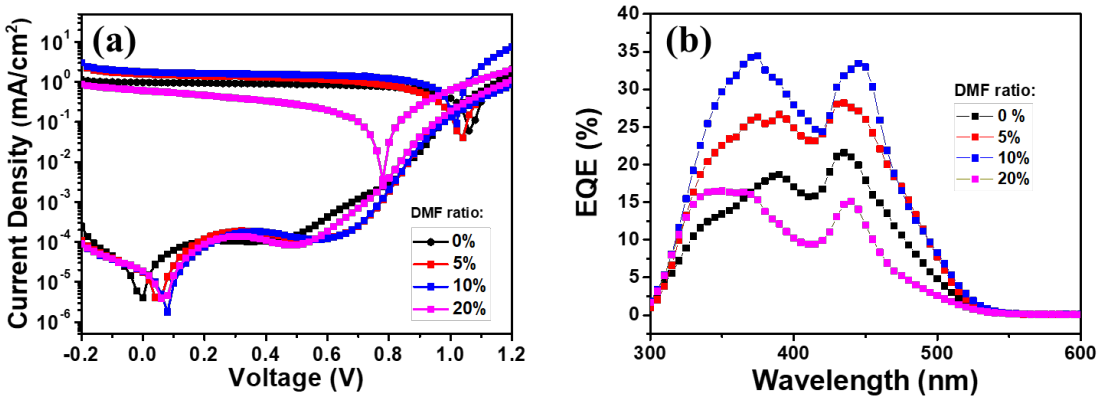

Figure S6 (a) Photocurrent and dark current density–voltage (J–V) curves of the $Cs_2AgBiBr_6$ photodetectors fabricated with different DMF ratio of 0%, 5%, 10% and 20%. (b) EQE curves of the $Cs_2AgBiBr_6$ photodetectors fabricated with different DMF ratio of 0%, 5%, 10% and 20% under 0 V bias.

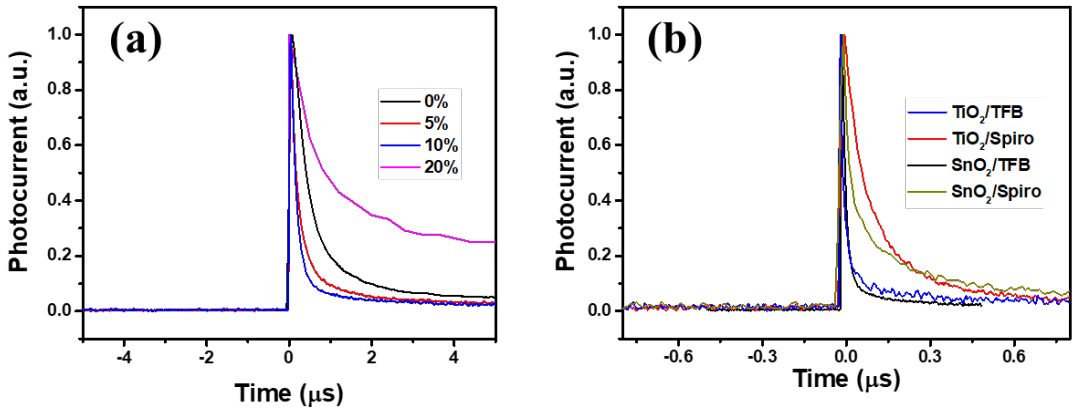

Figure S7 (a) Transient photocurrent of the $Cs_2AgBiBr_6$ photodetectors fabricated with different DMF concentrations 0%, 5%, 10% and 20%. (b) Transient photocurrent of the $Cs_2AgBiBr_6$ photodetectors based on different charge transport layers. (c) The trap density distribution of the $Cs_2AgBiBr_6$ photodetectors based on different charge transport layers and different $Cs_2AgBiBr_6$ films.

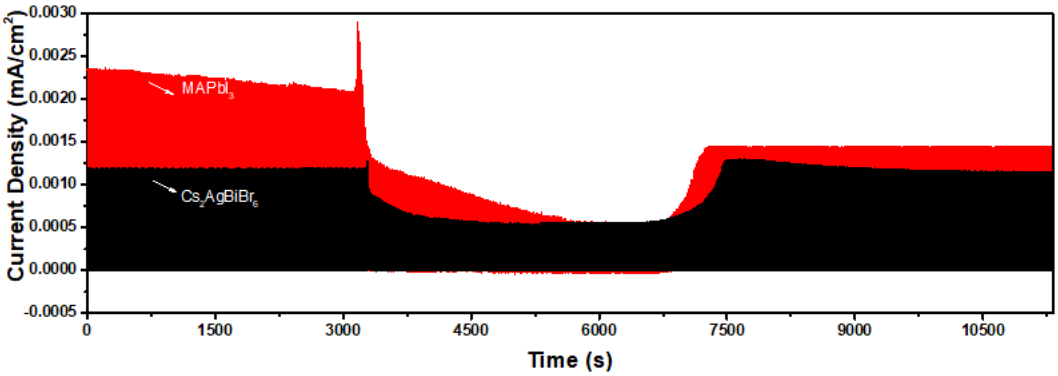

Figure S8 Thermal stability of the $Cs_2AgBiBr_6$ photodetector (black curve) and the $MAPbI_3$ photodetector (red curve) under light wavelength of 450 nm with the light intensity 10 μ W/cm^2 .